Unconventional magnetic order on the hyperhoneycomb Kitaev lattice inβ−Li2IrO3: full solution via magnetic resonant x-ray diffraction

A. Biffin, R. D. Johnson, Sungkyun Choi, Florian Freund, S. Manni, A. Bombardi, P. Manuel, Philipp Gegenwart, R. Coldea

Biffin, A., R. D. Johnson, Sungkyun Choi, Florian Freund, S. Manni, A. Bombardi, P. Manuel, Philipp Gegenwart, and R. Coldea. 2014. “Unconventional magnetic order on the hyperhoneycomb Kitaev lattice inβ−Li2IrO3: full solution via magnetic resonant x-ray diffraction.” *Physical Review B* 90 (20): 205116. https://doi.org/10.1103/physrevb.90.205116.

PHYSICAL REVIEW B **90**, 205116 (2014)

Unconventional magnetic order on the hyperhoneycomb Kitaev lattice in β-Li_2IrO_3: Full solution via magnetic resonant x-ray diffraction

A. Biffin,[1] R. D. Johnson,[1] Sungkyun Choi,[1] F. Freund,[2] S. Manni,[2] A. Bombardi,[3] P. Manuel,[4] P. Gegenwart,[2] and R. Coldea[1]
[1]*Clarendon Laboratory, University of Oxford, Parks Road, Oxford OX1 3PU, United Kingdom*
[2]*EP VI, Center for Electronic Correlations and Magnetism, Augsburg University, D-86159 Augsburg, Germany*
[3]*Diamond Light Source Ltd., Harwell Science and Innovation Campus, OX11 0DE, United Kingdom*
[4]*ISIS Facility, Rutherford Appleton Laboratory, Harwell Oxford, OX11 0QX, United Kingdom*
(Received 1 August 2014; revised manuscript received 6 October 2014; published 10 November 2014)

The recently synthesized iridate β-Li_2IrO_3 has been proposed as a candidate to display novel magnetic behavior stabilized by frustration effects from bond-dependent, anisotropic interactions (Kitaev model) on a three-dimensional "hyperhoneycomb" lattice. Here we report a combined study using neutron powder diffraction and magnetic resonant x-ray diffraction to solve the complete magnetic structure. We find a complex, incommensurate magnetic order with non-coplanar and counter-rotating Ir moments, which surprisingly shares many of its features with the related structural polytype "stripyhoneycomb" γ-Li_2IrO_3, where dominant Kitaev interactions have been invoked to explain the stability of the observed magnetic structure. The similarities of behavior between those two structural polytypes, which have different global lattice topologies but the same local connectivity, are strongly suggestive that the same magnetic interactions and the same underlying mechanism govern the stability of the magnetic order in both materials, indicating that both β- and γ-Li_2IrO_3 are strong candidates to realize dominant Kitaev interactions in a solid state material.

DOI: 10.1103/PhysRevB.90.205116 PACS number(s): 75.25.−j, 75.10.Jm

I. INTRODUCTION

Materials containing ions with a strong spin-orbit interaction are attracting much attention as candidates to display novel electronic states ranging from topological insulators with protected gapless surface states to quantum spin liquids with exotic excitations [1]. Complex magnetic behavior can arise when the strong spin-orbit coupling (as found for heavy transition metal 4*d* and 5*d* ions) and crystal field effects stabilize spin-orbit entangled magnetic moments, which may interact via anisotropic exchange interactions where the anisotropy axis depends on the bond orientation. On certain lattices these interactions may be strongly frustrated, leading potentially to novel forms of cooperative magnetic order and/or excitations, not found for magnets of 3*d* ions (where the spin-orbit coupling is much weaker and the orbital moment is in general quenched). The magnetic ground state of Ir^{4+} ions in a cubic IrO_6 octahedron is a doublet with a mixed spin-orbital character [2], $J_{\text{eff}} = 1/2$, and for edge-sharing IrO_6 octahedra it was proposed [3,4] that the leading superexchange is a ferromagnetic Ising coupling between the Ir magnetic moment components perpendicular to the Ir-O_2-Ir plane. For threefold coordinated, edge-sharing octahedra this leads to orthogonal Ir-O_2-Ir planes for the three Ir-Ir bonds coming out of each site and correspondingly orthogonal $\mathtt{x},\mathtt{y},\mathtt{z}$ components coupled along the three Ir-Ir bonds. For a honeycomb lattice this realizes the Kitaev model [5], where the strong frustration effects stabilize an (exactly solvable) quantum spin liquid state with novel excitations (Majorana fermions and fluxes) [6]. In the search for realizations of such physics, α-Na_2IrO_3 [7–11] and α-Li_2IrO_3 [12,13] have been actively explored experimentally, however no clear evidence of novel Kitaev phenomena has yet been observed.

Generalization of the Kitaev model to three-dimensional (3D) lattices has also been shown to have quantum spin liquid ground states [14–16]. Furthermore, nontrivial magnetic behavior has been predicted when (finite) additional interactions suppress the spin liquid and stabilize magnetic order [15,17]. The recently synthesized "hyperhoneycomb" [18] β-Li_2IrO_3 (see Fig. 1) and "stripyhoneycomb" [19] γ-Li_2IrO_3, which have the local connectivity of threefold coordinated IrO_6 octahedra with near-orthogonal Ir-O_2-Ir planes meeting at each Ir site, are prime candidates to realize 3D Kitaev physics. The availability of single-crystal samples of *both* of those two distinct structural polytypes offers unique opportunities to perform comparative studies between them and gain insight into the underlying physics. In recent experiments [20] on the γ polytype we have observed an unexpectedly complex, yet highly-symmetric incommensurate magnetic structure with non-coplanar and counter-rotating moments, and theoretical calculations showed that this structure could be stabilized by a spin Hamiltonian with dominant Kitaev couplings and some additional interactions. Here we extend our experimental studies to the β polytype, where we find some striking similarities in the magnetic structure. This shows that the key features of the magnetic order are robust, independent of the changes in the global lattice topology between the two distinct structural polytypes that share the same building blocks. This is strongly suggestive that the same underlying magnetic interactions govern the stability of the magnetic order in both structural polytypes, which would be an important constraint on any theoretical model of the cooperative magnetism in this family of materials.

The structural polytype β-Li_2IrO_3 was discovered by Takayama *et al.* [18] and the crystal structure is illustrated in Fig. 1 (left). It has an orthorhombic unit cell (space group $Fddd$, for full structural details see Appendix A) and the same mass density and same fundamental building blocks—edge-sharing LiO_6 and IrO_6 octahedra (the latter shaded in red)—as in the layered polytype α-Li_2IrO_3 [12], where edge-sharing IrO_6 octahedra form planar honeycomb layers separated by

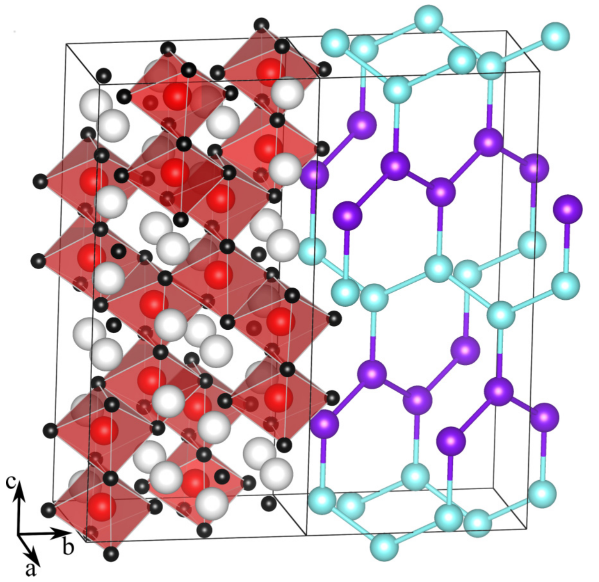

FIG. 1. (Color online) Crystal structure of β-Li_2IrO_3. Two unit cells are shown: (left) full structure with Li (white balls), O (black) and Ir (red) located inside IrO_6 octahedra (shaded polyhedra); (right) Ir ions are arranged in a "hyperhoneycomb" structure. Light (cyan) and dark (purple) colors indicate zigzag chains stacked along c and directed alternatingly along $\boldsymbol{a} \pm \boldsymbol{b}$.

hexagonal Li layers. In the β structure (see Fig. 1) the Ir lattice is threefold coordinated as in a planar honeycomb, but now the links of the lattice form a 3D network; this 3D lattice connectivity has been named a "hyperhoneycomb" [18]. It can be thought of as being made of zigzag chains [shaded cyan and purple in Fig. 1 (right)] stacked along c and alternating in direction between the two basal plane diagonals $\boldsymbol{a} \pm \boldsymbol{b}$ (the planar honeycomb structure is obtained when the zigzag iridium chains are *not* alternating in orientation, but are all running parallel to either the $\boldsymbol{a} + \boldsymbol{b}$, or the $\boldsymbol{a} - \boldsymbol{b}$ directions).

Earlier studies [18] have shown that β-Li_2IrO_3 is an insulator. The temperature-dependence of the magnetic susceptibility parameterized in terms of a Curie-Weiss law gave an effective magnetic moment $\mu_{\mathrm{eff}} = 1.61\mu_{\mathrm{B}}$, consistent with localized, $J_{\mathrm{eff}} = 1/2$ moments at the iridium sites. Both specific heat and susceptibility data showed an anomaly near $T_{\mathrm{N}} = 38$ K attributed to the onset of magnetic order. Here we confirm that the low-temperature phase has magnetic long-range order and we provide a full experimental magnetic structure solution. Our results give uniquely detailed information about the correlations that govern the cooperative magnetism and the relevant magnetic interactions that stabilize them. We first used neutron diffraction on a powder sample to confirm the presence of magnetic order at low temperatures and to obtain candidate magnetic propagation vectors. We then performed magnetic resonant x-ray diffraction (MRXD) experiments on a 17 μm diameter single crystal at the L_3 edge of iridium, where experiments on other iridates [2,8,21] have reported a strong enhancement of the magnetic scattering cross section. We exploit the polarization dependence of the MRXD intensity (probed via azimuth scans) to deduce that the magnetic structure has rotating magnetic moments and we determine the plane of rotation and relative phases between all 16 iridium sites in the structural unit cell.

The paper is organized as follows: Sec. II presents the neutron powder diffraction measurements and the analysis by which we obtain candidate magnetic propagation vectors. Sec. III A presents the single-crystal MRXD measurements, which observe magnetic Bragg peaks with an incommensurate propagation vector along the (100) direction. The observed diffraction pattern is analyzed in terms of magnetic basis vectors in Sec. III B and III C. The azimuth dependence of the diffraction intensity is used to determine the polarization of all magnetic basis vectors in the ground state and the relative phase between them (in Sec. III D). Finally the absolute value of the ordered magnetic moment is extracted from the neutron powder data in Sec. III E. The resulting magnetic structure is presented in Sec. III F and similarities with the magnetic structure in the γ polytype are discussed in Sec. IV. Finally, conclusions are summarized in Sec. V. Further technical details of the analysis are presented in the Appendices: (A) crystal structure refinement at low temperature from single-crystal x-ray data, (B) decomposition of the magnetic structure in terms of its Fourier components, (C) derivation of the selection rules for magnetic scattering for the various basis vectors, (D) the azimuth dependence of the MRXD intensity enabling determination of the relative phase between basis vectors, and (E) an equivalence mapping between the magnetic structures in the β and γ polytypes of Li_2IrO_3.

II. MAGNETIC NEUTRON POWDER DIFFRACTION

A. Experimental results

Neutron powder diffraction measurements to obtain information about the magnetic propagation vector were performed using the time-of-flight diffractometer WISH at the ISIS Facility (Rutherford Appleton Laboratory, Oxfordshire, UK). 0.71 g of powder β-Li_2IrO_3 (synthesized as described in Appendix A) was placed in an aluminium can of annular geometry (to minimize the strong neutron absorption by the Ir nuclei) and was mounted on the cold finger of a closed cycle refrigerator. Diffraction patterns were collected at a selection of temperatures from base (5.6 K) to paramagnetic (70 K), well above the magnetic ordering transition $T_{\mathrm{N}} = 38$ K inferred from thermodynamic measurements [18]. The obtained neutron diffraction pattern did not allow for a full structural refinement (most likely due to neutron absorption effects in the presence of iridium). We therefore performed additional x-ray measurements on a small single-crystal piece extracted from the same powder batch to determine precise internal atomic positions in the unit cell at a temperature of 100 K, considered to be cold enough to be representative of the crystal structure in the low-temperature limit. The x-ray diffraction was performed on a Mo-source Oxford Diffraction Supernova x-ray diffractometer under a N_2 gas flow, which gave a temperature of 100 K at the sample position. The data confirmed the expected space group and full structural refinement (for details see Appendix A) gave atomic positions consistent with those previously reported at room temperature [18].

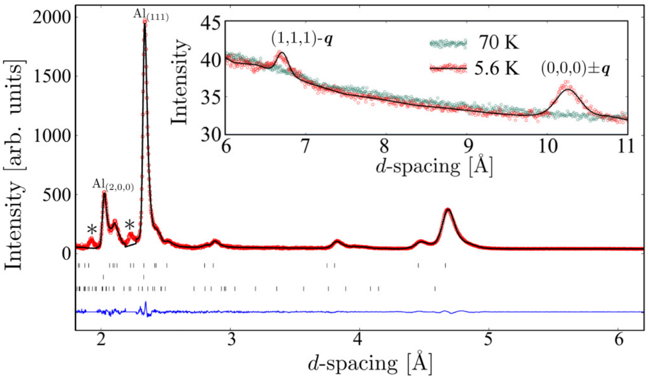

FIG. 2. (Color online) Neutron powder diffraction at base temperature (5.6 K, red circles) and in the paramagnetic regime (70 K, green circles) in the lowest-angle detector bank. Solid black line shows the fit to the structural and magnetic contributions as discussed in the text. Positions of structural β-Li_2IrO_3 peaks, aluminium peaks and magnetic Bragg peaks are marked below the pattern in the upper, middle and lower rows, respectively and the blue line underneath represents the difference between data and fit. Labels "Al" indicate aluminium peaks and (*) denote two peaks from an impurity phase identified as pure Ir, removed from the fit. Inset: zoom into the large d-spacing region showing two magnetic Bragg peaks, labels indicate the magnetic peaks index (symmetrically equivalent indexes are omitted).

Figure 2 shows the neutron powder diffraction pattern in the lowest angle bank of detectors, which covers the region of large d spacings where magnetic diffraction is expected. In the main panel the visible diffraction peaks are of structural origin. β-Li_2IrO_3 peak positions are denoted by the upper row of vertical marks (below the data) and the two large peaks in the data at d spacing near 2 Å (labeled "Al") are the lowest-order diffraction peaks from the Al can and were fitted as such. The pattern also showed two peaks labeled "$*$", originating from a small impurity phase identified as pure Ir, and those regions in the data were excluded from the analysis. We performed the structural fit (using FULLPROF [22]) to the neutron data (both paramagnetic and base temperature) with the internal atomic positions kept fixed, and only the lattice parameters left free to vary. The structural fit was consistent over all detector banks—corresponding to a range of scattering angles and resolutions—and we were also able to consistently fit the instrument parameters (which provide the conversion from time-of-flight to d spacing) over all the detector banks tested. Figure 2 illustrates the very good agreement in describing the structural diffraction pattern.

B. Candidate magnetic propagation vectors

The inset in Fig. 2 highlights the region of large d spacing, where upon cooling below T_N two new Bragg peaks appear, attributed to the onset of magnetic ordering. The peak widths are comparable to those of structural Bragg peaks, implying long-range magnetic order. With only two magnetic peaks the magnetic structure cannot be solved uniquely, however the data provides strong constraints on the magnetic propagation vector, $\boldsymbol{q}$. Typically $\boldsymbol{q}$ will lie on a point, line, or plane of high symmetry in the Brillouin zone. Using the *k-search* tool in FULLPROF [22] we systematically searched all such positions for the $Fddd$ space group in order of decreasing symmetry to find propagation vectors that could reproduce the magnetic peak positions observed in the powder neutron data. All commensurate orderings with wave vectors at the Γ, Z, Y, T and L points (where the Miller-Love convention for labeling high-symmetry Brillouin zone points has been used [23]) were ruled out by this analysis. Therefore we considered propagation vectors along lines of high symmetry with general points denoted by Σ, Δ, Λ. Only the first two were compatible with the neutron data, and the obtained solutions are listed in Table I, along with possible solutions for other high symmetry directions.

TABLE I. Candidate magnetic propagation vectors along high symmetry directions in the Brillouin zone compatible with the magnetic neutron powder diffraction pattern. The ellipses denotes the fact that multiple solutions exist for a general propagation vector in the ab plane.

Position	$\boldsymbol{q}_{\text{fit}}$
Σ	(0.57,0,0)
Δ	(0,0.81,0)
J	$(0.27,0,{}^1/_2)$
E	$(0,0.39,{}^1/_2)$
M	(0.43,0.53,0)
	⋮

III. MAGNETIC RESONANT X-RAY DIFFRACTION

A. Experimental results

To determine which of the candidate magnetic propagation wave vectors identified by the neutron data actually occurs, we have performed a magnetic resonant x-ray diffraction experiment in reflection geometry at the L_3 edge of Ir using the I16 beamline at Diamond (Diamond Light Source Ltd, Oxfordshire, UK). We used a single domain crystal of β-Li_2IrO_3 (characterized via x-ray diffraction as described in Appendix A) with an orthorhombic morphology with its maximum dimension less than 17 μm. The sample was placed on a Si (111) disk with the reciprocal lattice vector $(-6,5,7)$ being approximately surface normal and it was cooled using a closed-cycle refrigerator with Be domes. The x-ray energy was tuned to the L_3 edge of iridium (11.215 keV) and on cooling below T_N new Bragg peaks appeared at satellite positions of reciprocal lattice points at $(h,k,l) \pm \boldsymbol{q}$, with h,k,l integers and an incommensurate ordering wave vector $\boldsymbol{q} = (0.57(1),0,0)$. The magnetic origin of those peaks will be confirmed in several independent tests to be described later. Scans through such a peak are shown in Figs. 3(a)–3(c). The scans emphasize the incommensurate position along h and centering at integer k and l values. In the language of Table I this is then a propagation vector along the Σ line of symmetry, and the magnitude found from the x-ray data is consistent with the positions of peaks in the neutron data (first line in Table I). The incommensurate peaks are sharp in all three orthogonal reciprocal space directions and the peak shapes could be well described by Lorentzian squared profiles [fits shown by dashed

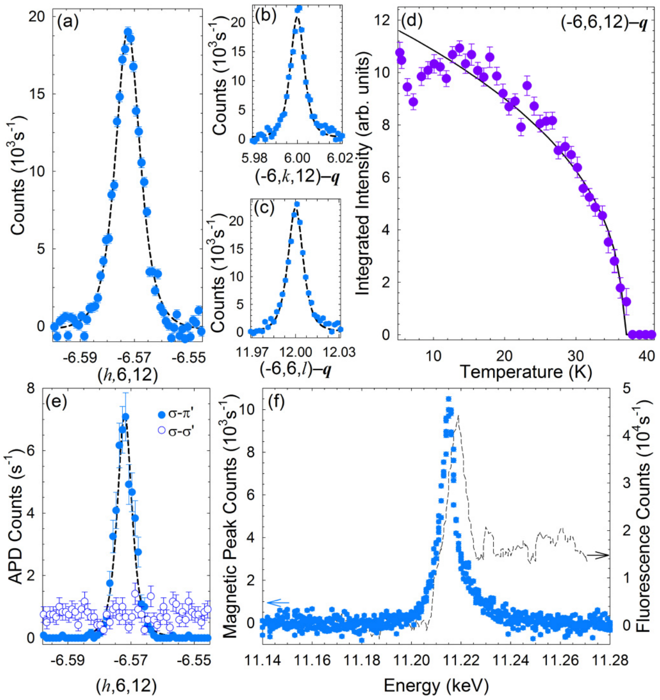

FIG. 3. (Color online) Magnetic Bragg peak at $(-6,6,12)-\boldsymbol{q}$. (a)–(c) Scans showing that the peak occurs along an incommensurate position along h, and is well centered at integer k and l; thick dashed lines are Lorentzian-squared fits. (d) Temperature dependence of the integrated peak intensity (the solid line is a power-law fit to extract T_{N}). (e) Scans with a polarizer in the scattered beam show that the peak is only present in the rotated polarization channel (σ-π') (light blue, filled) as expected for resonant magnetic scattering. (f) Intensity as a function of the x-ray energy (filled points) shows that the signal is resonant on the edge of the fluorescence signal onset (dashed line), as expected for resonant magnetic scattering.

lines in Figs. 3(a)–3(c) and 3(e)]. The inverse of the observed peak half-widths gives a lower bound on the correlation length estimated as 100, 200 and 300 Å along the a, b, and c axes, respectively (more than ≈20 unit cells in each direction). Those are comparable to values obtained from analyzing scans through a nearby structural Bragg peak $(-6,6,12)$, indicating no anomalous broadening of the magnetic peaks compared to structural peaks; i.e., the magnetic order is well developed and as long-range as the structural order.

Several independent tests can be performed to confirm the magnetic origin of the observed incommensurate diffraction peaks. Firstly, in Fig. 3(d) the integrated intensity of $(-6,6,12)-\boldsymbol{q}$ as a function of temperature (filled circles) shows a typical order-parameter behavior. A power-law fit (solid line) gives an onset temperature of $T_{\mathrm{fit}} = 36.7$ K, which is very close to the transition temperature deduced from specific heat measurements [18]. We attribute the apparent small offset of $\Delta T \simeq 1.3$ K to the fact that the sensor where the temperature was measured in the x-ray experiments was at the bottom of the sample support and the actual sample temperature may have been higher by ΔT due to local heating effects from the very intense synchrotron beam, a common occurrence in x-ray magnetic scattering experiments.

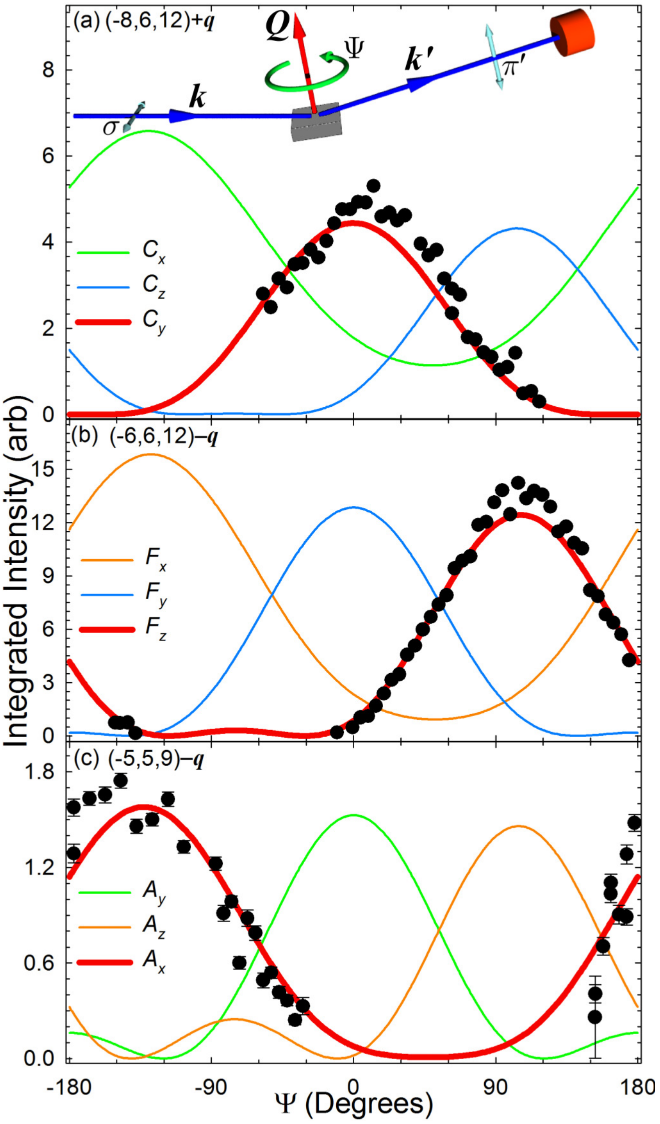

FIG. 4. (Color online) Intensity as a function of azimuth for three magnetic Bragg peaks (a) C_y, (b) F_z, and (c) A_x. The top diagram illustrates the scattering geometry. Data points (filled circles) are integrated peak intensities (in sample rocking curve scans) corrected for absorption and Lorentz factor. Thick (red) lines show fits that include all contributions to the magnetic scattering intensity [27] for the magnetic structure model Γ_4 depicted in Fig. 6. Orange, green, and blue lines denote other models ($\Gamma_{1,2,3}$, respectively, see Table II), which can be easily ruled out. The azimuth origin $\Psi = 0$ corresponds to the case when the (010) axis is in the scattering plane making the smallest angle with the incident beam direction $\hat{\boldsymbol{k}}$.

Further evidence of the magnetic origin of the incommensurate diffraction peaks can be obtained via polarization analysis of the scattered beam. For a scattering experiment with incident beam polarization $\hat{\boldsymbol{\epsilon}}$ normal to the $(\boldsymbol{k},\boldsymbol{k}')$ scattering plane (σ polarized), magnetic scattering is expected to rotate the polarization by 90° compared to the incident beam direction [scattering in the σ-π' channel; see diagram in Fig. 4(a) inset], whereas conventional (charge) scattering would leave the polarization direction unchanged (scattering in the σ-σ' channel) [24,25]. In the experiments polarization analysis was achieved via the third harmonic reflection from the (1,1,1) planes of an Au crystal, the d spacing of 0.785 Å being ideally suited for polarization analysis at the L_3 edge of Ir (giving perfect filtering at 11.16 keV; see Ref. [26]). Figure 3(e) shows an h scan across the incommensurate peak performed with polarizer parallel (open symbols, σ-σ') and perpendicular (filled symbols, σ-π') to the original incident beam polarization. The signal appears only in the rotated polarization channel, as expected for magnetic scattering. Note that the higher background in the σ-σ' channel is due to diffuse x-ray scattering, which is largely filtered out by the polarization analysis in the σ-π' channel revealing a pure magnetic signal.

A third test is the dependence on the x-ray energy, as the magnetic scattering is expected to undergo a strong enhancement at the absorption edge. Indeed, the incommensurate peak intensity has a characteristic resonant response as shown in Fig. 3(f) (filled blue symbols) with a maximum at the resonance energy of 11.215 keV in agreement with previous resonant studies on other iridates [8,21], and coincides with the edge of the fluorescence signal from the sample (black dotted line).

B. Magnetic basis vectors

The observation of incommensurate magnetic Bragg peaks indicates a moment-rotating or an amplitude-modulated structure with a periodicity that is incommensurate with the underlying crystal lattice. In order to distinguish between those two generic scenarios, and to determine the magnitude and orientation of the magnetic moments at all magnetic sites in the unit cell, we consider below symmetry-allowed basis vectors for magnetic structures with the observed propagation vector $\boldsymbol{q}$. This provides a natural framework to directly link diffraction data with a magnetic structure model and allows one to develop a systematic strategy in experiments to determine the magnetic structure completely.

The magnetic ions, Ir^{4+}, occupy a single crystallographic site with ions at $(1/8,1/8,z)$ [$z = 0.70845(7) \simeq 5/8 + 1/12$] and symmetry equivalent positions, giving four Ir ions in the primitive unit cell (labeled 1–4 in Fig. 6 and with positions listed explicitly in Table V in Appendix B). A natural way to describe the magnetic structure formed from the moments at these sites is through the language of basis vectors. The basis vectors contain symmetry-imposed relations between the Fourier components of the magnetic structure between the various sites in the primitive unit cell. In the present case four types of basis vectors can occur (as obtained using the *BasIReps* software [22]):

$$F = \begin{bmatrix} 1 \\ 1 \\ \delta \\ \delta \end{bmatrix}, \quad C = \begin{bmatrix} 1 \\ 1 \\ -\delta \\ -\delta \end{bmatrix}, \quad A = \begin{bmatrix} 1 \\ -1 \\ -\delta \\ \delta \end{bmatrix}, \quad G = \begin{bmatrix} 1 \\ -1 \\ \delta \\ -\delta \end{bmatrix}, \tag{1}$$

where for each vector the four values are relative phase factors between the Fourier components at the four magnetic sites in the primitive cell. $\delta = e^{-i\boldsymbol{q}\cdot(\boldsymbol{r}_3-\boldsymbol{r}_1)} = e^{-i\pi q/2}$ is a displacement phase factor that takes into account the fact that sites 3 and 4 are displaced relative to sites 1 and 2 by $a/4$ in the direction of the propagation vector $\boldsymbol{q}$. For example, in an F basis vector the Fourier components at the four sites are related by $\boldsymbol{M}_{\boldsymbol{q},1} = \boldsymbol{M}_{\boldsymbol{q},2} = \delta^{-1}\boldsymbol{M}_{\boldsymbol{q},3} = \delta^{-1}\boldsymbol{M}_{\boldsymbol{q},4}$, i.e., there are no additional phase factors between the four sites apart from the natural displacement phase factor, and in the limit $q \to 0$ ($\delta \to 1$) one recovers ferromagnetic order. For the basis vectors C, A, and G two out of the four sites have a change in sign in addition to the normal displacement phase factor, and in the limit $q \to 0$ one finds an antiferromagnetic alignment between the four sites. To determine the full magnetic structure, we first identify which basis vectors are present, determine their polarization (i.e., along the crystallographic axes x, y, or z) and then find the relative phase between them, as follows.

C. Selection rules for magnetic scattering

Each magnetic basis vector contains a strict, symmetry-imposed phase relation between the magnetic moments at the various sites in the primitive unit cell. As such, one can derive selection rules for nonzero magnetic diffraction intensity, i.e., each basis vector will only contribute to magnetic satellite reflections of certain reciprocal lattice points and will have zero structure factor for others. It follows that simply the presence or absence of magnetic Bragg peaks at certain positions can already identify which basis vectors are present.

Explicitly, the structure factor for a magnetic superlattice reflection at $\boldsymbol{Q} = (h,k,l) \pm \boldsymbol{q}$ is

$$\mathcal{F}(\boldsymbol{Q}) = \mathcal{F}((h,k,l) \pm \boldsymbol{q}) = f_F \sum_n \boldsymbol{M}_{\pm\boldsymbol{q},n} e^{i\boldsymbol{Q}\cdot\boldsymbol{r}_n}, \tag{2}$$

where the prefactor $f_F = 1 + e^{i\pi(h+k)} + e^{i\pi(k+l)} + e^{i\pi(l+h)}$ is due to the F-centering of the orthorhombic structural unit cell. The sum extends over all sites in the primitive cell ($n = 1$–4) and $\boldsymbol{M}_{\pm\boldsymbol{q},n}$ are the Fourier components of the magnetic moments at site n with position in the unit cell $\boldsymbol{r}_n$. Direct calculation of the structure factor (see Appendix C for details) for each of the four basis vectors in (1) gives the following selection rules. For an F basis vector magnetic scattering will occur at $\pm\boldsymbol{q}$ satellites of reciprocal lattice points (h,k,l) with the selection rule h,k,l all odd, or all even with $h + k + l = 4p$, p integer. This is the same selection rule as for structural Bragg scattering from the iridium ion sublattice at the (h,k,l) position, as expected since in the limit $q \to 0$ the F-type magnetic basis vectors recover ferromagnetic order, and this has the same selection rule as structural scattering. The resulting selection rule for an A basis vector is the same as for F, with the only difference that there is no contribution from A if $l = 6m$ and no contribution from F if $l = 3 + 6m$, m integer (for iridium at the "ideal" position $z = 5/8 + 1/12$). The selection rule for C and G is h,k,l all odd, or all even and $h + k + l = 4p + 2$, p integer, with no contribution from G if $l = 6m$ and no contribution from C if $l = 3 + 6m$, m integer.

The experimental geometry constrained the search for magnetic satellite reflections to regions of reciprocal space in the vicinity of the surface normal reflection, $\approx(-6,5,7)$. Using the above selection rules we ascertained 3 positions of interest for identifying which basis vectors contribute to the magnetic structure, namely $(-6,6,12) \pm \boldsymbol{q}$ (pure F), $(-8,6,12) \pm \boldsymbol{q}$ (pure C), and $(-5,5,9) \pm \boldsymbol{q}$ (mixed A and G) and found magnetic peaks at all these positions. Therefore we deduce that the structure contains F, C, and one (or both) of A and G. To determine the direction of the magnetic moment components for each of those basis vectors we make use of the polarization dependence of the magnetic x-ray diffraction intensity, as follows.

D. Azimuth scans to determine the moment's direction and relative phases between basis vectors

In the electric dipole approximation the magnetic x-ray diffraction intensity at resonance is proportional to

$$L(\theta)\mathcal{A}|(\hat{\boldsymbol{\epsilon}}' \times \hat{\boldsymbol{\epsilon}}) \cdot \boldsymbol{\mathcal{F}}(\boldsymbol{Q})|^2,$$

where $L(\theta)$ is the Lorentz factor at the scattering angle 2θ, $\mathcal{A}$ is an absorption correction dependent upon the angles between the incident and scattered beam directions and the normal to the crystal surface, $\boldsymbol{\mathcal{F}}(\boldsymbol{Q})$ is the magnetic structure factor vector given in (2), and $\hat{\boldsymbol{\epsilon}}'$ and $\hat{\boldsymbol{\epsilon}}$ are unit vectors along the polarization of the electric field component of the scattered and incident x-ray beams, respectively [24,25]. For a σ-polarized incident beam magnetic resonant scattering occurs only in the σ-π' channel [see diagram in Fig. 4(a) inset], meaning that the product of the electric field polarization vectors is along the scattered beam direction, i.e., $\hat{\boldsymbol{\epsilon}}' \times \hat{\boldsymbol{\epsilon}} = \hat{\boldsymbol{k}}'$, so only the component of the structure factor vector along the scattered beam direction, $\mathcal{F}_{\parallel} = \boldsymbol{\mathcal{F}} \cdot \hat{\boldsymbol{k}}'$, contributes to the magnetic intensity. By keeping the instrument in the scattering condition and rotating the sample around the scattering wave vector, $\boldsymbol{Q} = \boldsymbol{k}' - \boldsymbol{k}$, the projection $\mathcal{F}_{\parallel}$ of the structure factor vector onto the (fixed) direction $\hat{\boldsymbol{k}}'$ varies depending on the azimuth angle Ψ, with maximum magnetic intensity when the magnetic moments that give rise to the scattering make the smallest angle with $\hat{\boldsymbol{k}}'$ and zero intensity when they are perpendicular.

Azimuth scans to test the polarization dependence are shown in Figs. 4(a)–4(c) where the data points are obtained by integrating the magnetic peak intensity in sample rocking curve scans for each value of the azimuth, Ψ. As discussed earlier, the selection rules identify the signal in panel (a) at $(-8,6,12) + \boldsymbol{q}$ to be of C character, and the observed maximum intensity at $\Psi = 0$ uniquely identifies the polarization to be along the y axis (red thick line) as at $\Psi = 0$ the y axis is in the scattering plane and makes the smallest angle with the $\hat{\boldsymbol{k}}'$ direction and makes a larger angle with $\hat{\boldsymbol{k}}'$ when the azimuth is displaced away from 0 in both directions; green and blue curves show the expected intensity dependence for other polarizations that can be clearly ruled out. Similarly, in panel (b) the peak at $(-6,6,12) - \boldsymbol{q}$ is identified as being of F character and polarized along z (thick red line). Panel (c) shows data at $(-5,5,9) - \boldsymbol{q}$, clearly of x polarization (thick red line). The structure factor is compatible with both an A or G character and we will show later that only a pure A character can describe this and other azimuth scans quantitatively, so we identify this peak as coming from an A_x basis vector.

The next step in solving the structure is to determine the relative phase between the A_x, C_y, and F_z basis vectors. A phase of 0 or π between basis vectors with orthogonal components, say along A_x and F_z, means that the moments vary sinusoidally along a direction in the xz plane, whereas a phase offset of $\pi/2$ means that the moments rotate in the xz plane describing an elliptical envelope with principal axes along x and z. The relative phase between two basis vectors can be determined from an azimuth scan at a magnetic Bragg peak position where both basis vectors contribute, as the intensity is the sum of the intensities due to the two separate basis vectors plus an additional cross-term that is sensitive to the phase offset (for more details see Appendix D).

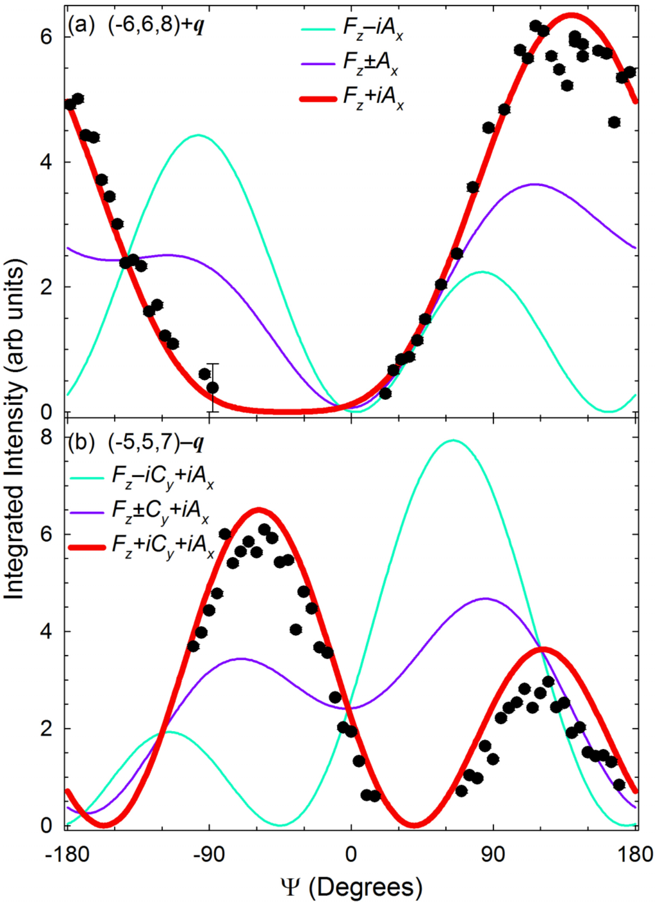

FIG. 5. (Color online) Intensity as a function of azimuth for "mixed" magnetic Bragg peaks (black circles) corrected for absorption and Lorentz factor, compared to calculations (red thick line) for the magnetic structure model in Fig. 6, as well as calculations for other possible models: (a) $(-6,6,8) + \boldsymbol{q}$ is a mixed F:A peak with contributions in the ratio 1:3, (b) $(-5,5,7) - \boldsymbol{q}$ is a mixed F:C:A peak with contributions in the ratio 3:3:1. Note that the data clearly distinguishes between different relative phases of basis vectors (cyan and purple).

Figure 5(a) shows the azimuth scan at $(-6,6,8) + \boldsymbol{q}$ where structure-factor calculations show that both F and A basis vectors contribute in the ratio $1:3$. The intensity dependence uniquely identifies it as originating from the particular basis vector combination $F_z + iA_x$, i.e., the x components are $\pi/2$ out of phase with respect to the z components, meaning that the magnetic moments rotate in the xz plane (in a particular sense on each site, note that the opposite sense of rotations encoded in the basis vector $F_z - iA_x$ is not consistent with the data; cyan line). The data clearly rules out the case when the moments are not rotating in the xz plane, but are varying sinusoidally along a line in the xz plane ($F_z \pm A_x$, purple line), a model with no A_x component is also ruled out (not shown).

TABLE II. Irreducible representations and basis vectors for a magnetic structure with propagation vector $\boldsymbol{q} = (q,0,0)$.

Irreducible representation	Basis vectors
Γ_1	F_x, G_y, A_z
Γ_2	C_x, A_y, G_z
Γ_3	G_x, F_y, C_z
Γ_4	A_x, C_y, F_z

This analysis shows that an A_x basis vector must exist in the ground state and that it is $\pi/2$ out of phase with respect to F_z. Similarly, to determine the phase offset between the F_z and C_y basis vectors we measured the azimuth scan at the magnetic reflection $(-5,5,7) - \boldsymbol{q}$ of mixed F, C, and A contributions in the ratio 3 : 3 : 1, shown in Fig. 5(b), and only a model with the basis vector combination $F_z + iC_y + iA_x$ (thick red line) matches the data, with other tested combinations (blue and green curves) clearly ruled out.

We have also tested for the possibility that the relative phase between the basis vectors A_x and F_z, and between C_y and F_z, might be different from the special values of 0, $\pm\pi/2$, and π, however allowing those relative phases to vary continuously gave no improvement in the fit to the data compared to the case where the phases were fixed at $\pi/2$ (thick red line in Fig. 5) and in fact values different from $\pm\pi/2$ can be ruled out theoretically as they would lead to a magnetic structure that is not compatible with the symmetry of the crystal structure (for details see Appendix B).

Having established all the basis vectors that are present, their polarization, and their relative phases, the relative magnitudes are obtained by quantitatively fitting the azimuth intensity dependencies. Three free parameters were fit; the relative ratios M_x/M_z and M_y/M_z, and a *single* overall intensity scale factor for all the data. The simultaneous fit of this magnetic structure model to the data in Figs. 4(a)–4(c), 5(a), and 5(b) (shown by the thick red solid lines) gave the moment amplitudes in the relative ratio $M_x : M_y : M_z = 0.45(1) : 0.65(1) : 1$. Note that the basis vector combination (iA_x, iC_y, F_z) with the above moment amplitudes quantitatively explains the mixed F_z, A_x peak in Fig. 5(a), and the *same* magnitude A_x basis vector also quantitatively accounts for the azimuth dependence in Fig. 4(c), further confirming the identification of the signal in this magnetic Bragg peak as coming from a pure A_x basis vector [if a G_x basis vector is also present and contributing to the signal in Fig. 4(c), its magnitude is very small, below the accuracy of the present experiments]. Given this we conclude that the magnetic structure is described by the basis vector combination (iA_x, iC_y, F_z), which corresponds to a single irreducible representation, Γ_4, in Table II.

E. Absolute value of the ordered moment

The only remaining parameter still to be determined is the absolute magnitude of the magnetic moments. This is difficult to extract reliably from the magnetic resonant x-ray diffraction data as it requires accurate determination of scale factors between the magnetic and structural peaks (the latter being of order 10^5–10^6 more intense). However, in neutron scattering experiments the magnetic and structural peaks are of comparable magnitudes and one can obtain a reliable determination of the relative scale factor. To this aim we return to the powder neutron data in Fig. 2 and simultaneously fit three contributions to the data: structural peaks of the sample calculated using the crystal structure with fixed internal parameters (as deduced from single crystal x-ray diffraction), aluminium structural peaks (from the sample can), and magnetic peaks. For the magnetic contribution a single scale factor was fitted using the magnetic structure model deduced from the resonant x-ray data with the basis vector combination (iA_x, iC_y, F_z) with fixed magnitude ratios M_x/M_z and M_y/M_z. The fit is plotted as a solid black line in Fig. 2 and shows excellent agreement with the data. The resulting ordered magnetic moment magnitude is $0.47(1)\mu_{\mathrm{B}}$ when aligned along the c axis. The propagation vector was also fitted and we find $\boldsymbol{q} = (0.5768(3),0,0)$, consistent with the x-ray measurements.

F. Magnetic structure

Having determined the magnetic basis vectors, their amplitudes, and relative phases, the magnetic structure in real space is obtained via a Fourier transformation as described in Appendix B. The obtained magnetic structure projected onto the ac plane is shown in Fig. 6(a). The magnetic moments are counter-rotating between all nearest-neighbor sites, and the plane of rotation alternates between the two sites of every vertical (c-axis) bond as illustrated by the pattern of light and dark shaded elliptical envelopes. The planes of rotation are obtained from the ac plane by rotation around the c axis by an angle $\pm\phi$, with $\phi = \tan^{-1}\frac{M_y}{M_x} = 55(1)^\circ$. Each zigzag chain has the top and bottom sites counter-rotating in one and the same plane, which then alternates between consecutive zigzag chains vertically linked along the c axis. The zigzag chains are directed alternatingly along the $\boldsymbol{a} \pm \boldsymbol{b}$ directions and are made up of iridium sites of type (2,4) and (1,3), respectively, with vertical (c-axis) bonds coupling sites of types 1-2 and 3-4. The magnetic order pattern is such that for every vertical bond the spin components along the y axis are ferromagnetically aligned (see Fig. 7), in accordance with the basis vector C_y, which has equal Fourier components at sites 1-2 and 3-4, respectively [see Eq. (1)].

We note that the magnetic moment rotation at each site defines an elliptical envelope, distorted from circular with the moment reduced by ~20% when in the ab plane compared to when along the c axis, $\sqrt{M_x^2 + M_y^2}/M_z = 0.80(1)$. This effect may be due to a larger g factor along the c axis compared to the $\hat{\boldsymbol{a}} \cos\phi \pm \hat{\boldsymbol{b}} \sin\phi$ directions in the ab plane. We note that single-crystal susceptibility data [19] in the related polytype γ-$\mathrm{Li_2IrO_3}$ do provide evidence for the presence of g-tensor anisotropy for the iridium moments (in the high-temperature limit the susceptibility, χ, is expected to be proportional to the squared g factor along the applied field direction, and experiments observe χ_c larger than both χ_a and χ_b, implying an anisotropic g tensor). The very similar local environment around the iridium sites in β-$\mathrm{Li_2IrO_3}$ suggests that an anisotropic g tensor is also likely here. Another possibility is that zero-point quantum fluctuations may prefer a non-fixed-length ordered moment between sites, with a larger ordered moment along the c axis, which is the only direction that is common to all planes of rotation. Evidence for the

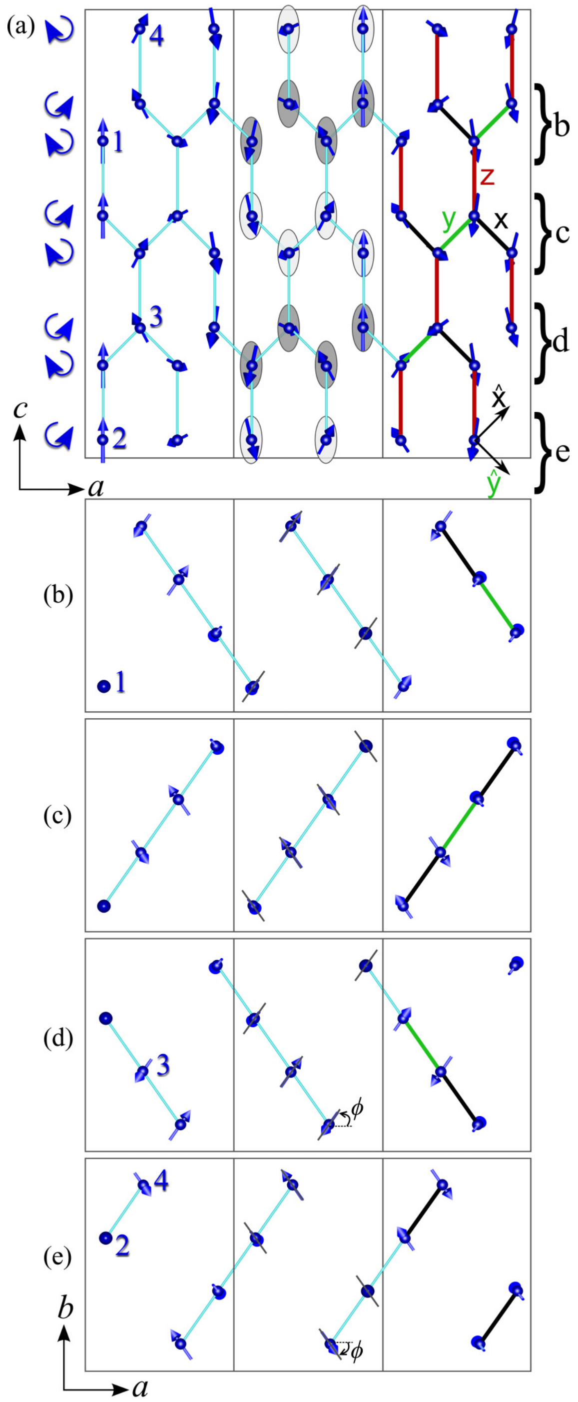

FIG. 6. (Color online) (a) Projection of the magnetic structure on the *ac* plane showing the sites 1–4 of the primitive cell. Left curly arrows indicate counter-rotation of moments between consecutive sites along *c*. In unit cell 2 light and dark shaded elliptical envelopes indicate an alternating tilt of the plane of moments' rotation away from the *ac* face. In unit cell 3 the color of bonds shows the anisotropy axis of the exchange in a Kitaev model [15] (ferromagnetic Ising exchange for each bond, but with a different Ising axis x,y,z for the black/green/red bonds). Right-hand labels (b)–(e) indicate where slices through the magnetic structure are taken at different heights in the unit cell and projected onto the *ab* plane to illustrate the direction of the zigzag chains and the alternating tilt of the plane of rotation away from the *ac* plane by $\pm\phi$ between adjacent zigzag chains stacked along *c*.

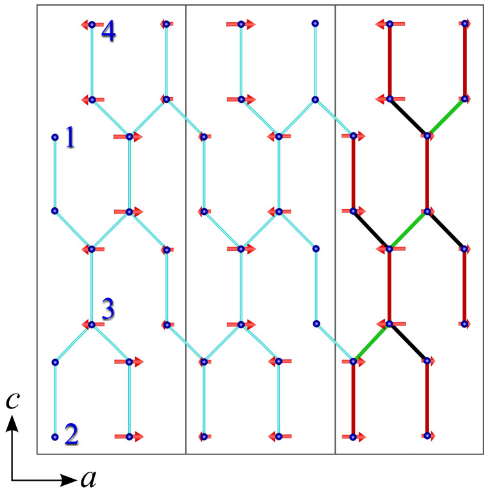

FIG. 7. (Color online) Projection of the iridium lattice on the *ac* plane showing the ordering of the magnetic moment components along the *b* axis only. Those are shown rotated (for ease of visualization) from the *b* to the *a* axis and indicated by horizontal red arrows (length of arrow indicates the *b*-axis moment component at each site). Note the ferromagnetic alignment between the two sites of each vertical (*c*-axis) bond.

presence of zero-point quantum fluctuations in the ground state is provided by the fact that the absolute magnitude of the ordered moment [0.47(1) μ_B] is significantly reduced from what is believed to be the available full-moment value (estimated at $g\mu_B J_{\text{eff}} \simeq 1\mu_B$ assuming $g \simeq 2$), so a structure with small modulations on an already significantly reduced ordered moment could be compatible with the experimental results.

IV. DISCUSSION

It is interesting to note that the obtained magnetic structure has striking similarities with the magnetic structure in the related polytype γ-Li_2IrO_3 [20], with which β-Li_2IrO_3 shares the same size orthorhombic unit cell ($a \times b \times c$) and also many key structural features. In both polytypes the iridium lattice is locally threefold coordinated and is made up of vertically linked zigzag chains that alternate in orientation between the $\boldsymbol{a} \pm \boldsymbol{b}$ direction. The only difference between them is that in the hyperhoneycomb β polytype this alternation occurs between consecutive zigzag chains, whereas in the stripyhoneycomb γ polytype the alternation occurs between pairs of parallel zigzag chains (which form a honeycomb row). The magnetic structures in both polytypes are incommensurate with the same propagation vectors within experimental error, $\boldsymbol{q} = (0.57(1),0,0)$, the moments are counter-rotating between the sites of every nearest-neighbor bond, and the plane of rotation alternates between two orientations tilted away (by an angle ϕ) from the *ac* plane between consecutive zigzag iridium chains vertically linked along the *c*- axis. The ϕ angle was found to be somewhat smaller in γ-Li_2IrO_3, but apart from this difference the magnetic structure in γ-Li_2IrO_3 can be regarded as "equivalent" to that in β-Li_2IrO_3 but in a different lattice setting (for a formal mapping see Appendix E). Those similarities are strongly suggestive that the defining features of the magnetic structure, namely non-coplanarity, the counter-rotation on every nearest-neighbor bond, and the direction and even the magnitude of the incommensurate ordering wave vector, are determined by the same type of short-range magnetic interactions in both polytypes, and those features appear to be robust against changes in the global lattice connectivity (i.e., how zigzag chains are vertically linked in a long-range pattern) which leave the local connectivity of the zigzag chains unchanged. In the γ polytype it was shown [20] that the key features of the magnetic order can be stabilized by a spin Hamiltonian with dominant Kitaev couplings with some additional interactions; the observation of similar magnetic structures in the β and γ polytypes suggests the same underlying magnetic interactions occur in both cases. The relevant parent Kitaev model for the β-polytype has been considered in Refs. [15,16] and is illustrated in Fig. 6(a) (unit cell 3). Here the color of the bonds indicates the anisotropy axis of the exchange, i.e. for the each Ir-Ir bond there is a ferromagnetic Ising coupling between the components normal to the Ir-O_2-Ir plane of that bond. There are three reciprocally-orthogonal Ir-O_2-Ir planes meeting at each site and their normal directions define a set of orthogonal axes denoted by the sans serif symbols x, y and z (to distinguish them from the italicized symbols x, y, z used to denote the orthorhombic axes directions). The Kitaev and crystal axes are related by $\hat{\mathsf{x}} = (\hat{\boldsymbol{a}} + \hat{\boldsymbol{c}})/\sqrt{2}$, $\hat{\mathsf{y}} = (\hat{\boldsymbol{a}} - \hat{\boldsymbol{c}})/\sqrt{2}$ and $\hat{\mathsf{z}} = \hat{\boldsymbol{b}}$ (where we have assumed the parent "idealized" lattice with cubic IrO_6 octahedra and $a : b : c = 1 : \sqrt{2} : 3$). We note that the magnetic interactions may also be very similar in magnitude between the β and γ polytypes, as they show very similar values for the magnetic ordering temperature. Table III summarizes the magnetic parameters of all three structural polytypes of Li_2IrO_3 including the layered honeycomb α phase, for which powder neutron diffraction experiments [28] have also revealed evidence for an incommensurate long-range magnetic order. It will be interesting to explore in detail experimentally the magnetic structure in the layered honeycomb and compare with the magnetic structure in the three-dimensional β and γ lattices to develop a systematic understanding of how the magnetism evolves between all three structural polytypes, which share the same threefold local connectivity, but with a different global lattice topology.

TABLE III. Summary of experimentally available magnetic parameters of the three structural polytypes of Li_2IrO_3: Curie-Weiss temperature θ_{CW} and effective magnetic moment μ_{eff} deduced from high-temperature susceptibility data, magnetic ordering temperature T_N, magnitude of the ordered magnetic moment $\langle\mu_{ord}\rangle$ (along c) and non-coplanar tilt ϕ of the moments' rotation plane in the ordered phase.

Polytype	θ_{CW} (K)	μ_{eff} (μ_B)	T_N (K)	$\langle\mu_{ord}\rangle$ (μ_B)	ϕ (deg.)
α	−33[a]	1.83[a]	15[a]		
β	40[b]	1.61[b]	38[b]	0.47	55
γ		1.6[c]	39.5[d]		42[d]

[a] Reference [13].

[b] Reference [18].

[c] Reference [19].

[d] Reference [20].

V. CONCLUSIONS

We have reported a combined study using magnetic neutron powder diffraction and single-crystal magnetic resonant x-ray diffraction experiments at the L_3 edge of Ir to explore the magnetic structure of β-Li_2IrO_3, which is a unique realization of a hyperhoneycomb iridium lattice, a candidate to display 3D Kitaev physics of strongly frustrated, bond-anisotropic interactions. Using the azimuth dependence of the magnetic Bragg peak intensities combined with magnetic symmetry analysis we have obtained a complete solution for the magnetic structure for all 16 iridium sites in the structural unit cell. We find an incommensurate, non-coplanar magnetic structure with moments counter-rotating on every nearest-neighbor bond. The magnetic structure shows striking similarities to the magnetic structure of the related structural polytype γ-Li_2IrO_3, suggesting that the same underlying Hamiltonian (with dominant Kitaev interactions) stabilizes the defining features of the magnetic structure in both structural polytypes.

ACKNOWLEDGMENTS

Work at Oxford was supported by EPSRC (UK) under Grants No. EP/H014934/1 and No. EP/J003557/1, and at Diamond and ISIS by STFC (UK). Work at Augsburg was supported by the Helmholtz Virtual Institute 521 ("New states of matter and their excitations").

APPENDIX A: SAMPLE SYNTHESIS, CHARACTERIZATION, AND LOW-TEMPERATURE STRUCTURAL REFINEMENT

The synthesis route to obtain the samples used in the neutron and x-ray experiments was as follows. First, a powder sample of the layered honeycomb phase α-Li_2IrO_3 was prepared as described in Ref. [13]. Then repetitive annealing at 1100 °C transformed the sample into hyperhoneycomb β-Li_2IrO_3, confirmed via powder x-ray diffraction. Bulk magnetic susceptibility and heat capacity measurements on the powder sample indicated evidence for magnetic ordering at 38 K, in full agreement with Ref. [18]. The polycrystalline powder contained small shiny crystallites. Several such crystallites were extracted from the powder and their diffraction pattern measured using a Mo source single-crystal SuperNova x-ray

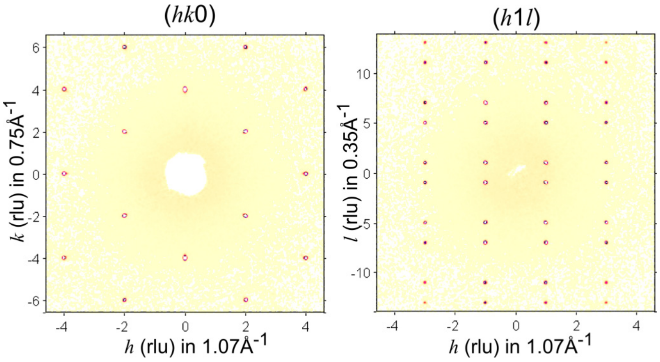

FIG. 8. (Color online) X-ray diffraction pattern at 300 K in the (hk0) and (h1l) planes from the crystal used in the resonant x-ray diffraction experiments.

TABLE IV. β-Li_2IrO_3 structural parameters at 100 K.

Cell parameters

Space group: $Fddd$ (no. 70, origin choice 2)

$Z = 16$

a,b,c (Å):	5.8903(2)	8.4261(3)	17.7924(7)
α,β,γ:	90°	90°	90°

Volume (Å^3): 883.08(6)

Atomic fractional coordinates and isotropic A.D.P.'s

Atom	x	y	z	U_{iso} (Å^2)
Ir	0.125	0.125	0.70845(7)	0.0025(3)
Li1	0.125	0.125	0.04167	0.00633
Li2	0.125	0.125	0.875	0.00633
O1	0.855(7)	0.125	0.125	0.002(5)
O2	0.621(8)	0.3669(19)	0.0384(7)	0.002(3)

Data collection

No. of measured reflections: 3770

Data reduction R_{int}: 6.99%

[Criterion for observed reflections: $I > 2.0\sigma(I)$]

No. of observed independent reflections: 298

No. of fitted parameters: 9

diffractometer. Representative diffraction patterns in the $(hk0)$ and $(h1l)$ planes obtained from the sample used in the magnetic resonant x-ray diffraction experiments (diameter 17 μm) are shown in Fig. 8. The patterns observe sharp Bragg peaks, indicating a high-quality single crystal, with selection rules consistent with the $Fddd$ space group expected for β-Li_2IrO_3. The results of the full structural refinement of a complete x-ray diffraction data set collected at 100 K from another crystal of comparable dimensions from the same batch are given in Table IV, where we have used the same convention for the origin of the unit cell as in Ref. [18]. In the table A.D.P. stands for atomic displacement parameters, which were assumed to be isotropic. The reliability factors of the Rietveld refinement were $R(F^2) = 4.50\%$, $wR(F^2) = 5.24\%$, $R(F) = 2.42\%$, and $\chi^2 = 0.318$.

APPENDIX B: MAGNETIC SYMMETRY ANALYSIS

This section gives further details of the magnetic symmetry analysis and the description of the magnetic structure using basis vectors. The iridium ions occupy a single crystallographic site, $16g$ $(1/8,1/8,z)$, $z = 0.70445(7)$, with four iridium sites per primitive cell [labeled 1–4 in Fig. 6(a) (left panel)] with coordinates listed in Table V.

TABLE V. Fractional atomic coordinates of the iridium sites in the primitive cell and corresponding magnetic basis vector components in the determined magnetic structure.

Site	Coordinates	v_x	v_y	v_z
1	$(0.125,0.125,z)$	+	+	+
2	$(0.125,0.625,3/4-z)$	−	+	+
3	$(0.375,0.375,1-z)$	−	−	+
4	$(0.375,0.875,1/4+z)$	+	−	+

Taking into account that at each site the magnetic moment could have components along the x, y, and z axes (along the orthorhombic a, b, c axes), gives a 12-component representation of the (restricted) space group $G_{\boldsymbol{q}}$ formed by the symmetry elements of the full space group that leave the propagation vector $\boldsymbol{q}$ invariant. $G_{\boldsymbol{q}}$ contains a twofold axis $2(x,3/8,3/8)$ and diamond glide planes in the xy and xz planes, $d(1/4,1/4,0)$ and $d(1/4,0,1/4)$. The irreducible representations and associated magnetic basis vectors (obtained using the *BasIReps* tool, part of the FULLPROF suite [22]) are listed in Table II. The magnetic basis vectors, F, C, A and G listed in (1) encode symmetry-imposed relations between the Fourier components, $\boldsymbol{M}_{\boldsymbol{q},n}$, of the magnetic moments at the four sites, $n = 1$–4, in the primitive cell. The (real) magnetic moments are expressed in terms of the Fourier components as $\boldsymbol{M}_{\boldsymbol{r},n} = \sum_{\boldsymbol{k}=\pm\boldsymbol{q}} \boldsymbol{M}_{\boldsymbol{k},n} e^{-i\boldsymbol{k}\cdot\boldsymbol{r}}$, where $\boldsymbol{M}_{-\boldsymbol{q},n} = \boldsymbol{M}^*_{\boldsymbol{q},n}$ as the magnetic moment distribution is real.

Symmetry operations of the full space group that map $\boldsymbol{q}$ into $-\boldsymbol{q}$ (in the preset case a twofold axis at the iridium sites) impose further constraints onto the allowed values for the relative phases between basis vectors corresponding to the same irreducible representation. In particular for the Γ_4 representation in Table II, the only allowed basis vector combinations (obtained using the ISODISTORT [29] software) are $(\pm iA_x, \pm iC_y, F_z)$. The experimentally determined magnetic basis vectors are found to all belong to the representation Γ_4 and occur in one of the symmetry-allowed combinations above, namely (iA_x, iC_y, F_z) with magnitudes M_x, M_y, and M_z. Using the definition of the magnetic basis vectors in (1) the Fourier components of the magnetic structure are then obtained as

$$\boldsymbol{M}_{\boldsymbol{q},n} = \left\{ i \left[\hat{\boldsymbol{x}} \frac{M_x}{2} v_x(n) + \hat{\boldsymbol{y}} \frac{M_y}{2} v_y(n) \right] + \hat{\boldsymbol{z}} \frac{M_z}{2} v_z(n) \right\} \times e^{-i\boldsymbol{q}\cdot(\boldsymbol{r}_n - \boldsymbol{r}_1)}, \tag{B1}$$

where $\hat{\boldsymbol{x}}$, $\hat{\boldsymbol{y}}$, $\hat{\boldsymbol{z}}$ are unit vectors along the orthorhombic $\boldsymbol{a}$, $\boldsymbol{b}$, $\boldsymbol{c}$ axes, respectively. The prefactors $v_{x,y,z}$ are obtained from the basis vectors along the corresponding axes, but without the displacement phase factors $e^{-i\boldsymbol{q}\cdot(\boldsymbol{r}_n-\boldsymbol{r}_1)}$, i.e., $v_x = [+--+]$ (from A_x), $v_y = [++--]$ (from C_y) and $v_z = [++++]$ (from F_z). From the Fourier components the magnetic moment at position $\boldsymbol{r}$ belonging to site index $n = 1$–4 is obtained as

$$\boldsymbol{M}_{\boldsymbol{r},n} = \hat{\boldsymbol{x}} M_x v_x(n) \sin \boldsymbol{q}\cdot\boldsymbol{r} + \hat{\boldsymbol{y}} M_y v_y(n) \sin \boldsymbol{q}\cdot\boldsymbol{r} + \hat{\boldsymbol{z}} M_z v_z(n) \cos \boldsymbol{q}\cdot\boldsymbol{r}. \tag{B2}$$

The above equation describes all iridium sites, including those related by F-centering translations, where $\boldsymbol{r}$ is the actual position of the ion and n is the site index at the equivalent position (1–4) in the primitive unit cell. The magnetic structure is plotted in Fig. 6 and corresponds to rotating magnetic moments at each site describing an elliptical envelope with a principal axis along c.

We note that the magnetic structure is fully compatible with the local 2_z rotation axis at the iridium sites, in particular the structure is invariant under the 2_z rotation applied at an iridium site where the magnetic moment is aligned along c. A magnetic structure where the elliptical envelope was tilted away from the c axis (corresponding to a relative phase between the A_x and

F_z, or C_y and F_z basis vectors displaced away from the nominal value of $\pm\pi/2$, i.e., a complex prefactor in front of A_x or C_y not equal to $\pm i$) would not be invariant under the 2_z rotation, so would not be symmetry allowed. In general, the symmetry constraint imposed by the twofold axis is such that, for a magnetic structure with all basis vectors belonging to a single irreducible representation $\Gamma_{1\text{–}4}$ in Table II, the components along the x and y axes are in phase or antiphase, and $\pm\pi/2$ out of phase with respect to the z components, and no other phase combinations are symmetry allowed. Consequently, each of the four irreducible representations $\Gamma_{1\text{–}4}$ can accommodate a magnetic structure with rotating moments describing an elliptical envelope with a principal axis along c, with counter-rotation in the (ac) plane between every nearest-neighbor pair of sites, non-coplanar with two orientations for the elliptical plane (obtained by rotations around the c axis by equal and opposite angles) with the only difference between the different representations being in the symmetry of the order pattern, i.e., the relative orientation of the moments between the different sites in the unit cell. Interestingly, examples of such magnetic structures in the Γ_1 and Γ_2 representations have been very recently considered theoretically in Ref. [17]: the so-called SP_{a^-} and SP_{a^+} structures, described in the shorthand notation of Table II (with $q = 1 - Q$, where Q is the ordering wave vector in the notation of Ref. [17]) as $\Gamma_1 : (iF_x, iG_y, A_z)$ and $\Gamma_2 : (iC_x, -iA_y, G_z)$, respectively; these two structures also have non-coplanar moments with counter-rotation in the (a,c) plane, but in a pattern with a different symmetry compared to the structure $\Gamma_4 : (iA_x, iC_y, F_z)$ plotted in Fig. 6 (in the former two cases the x components of the moments are parallel between successive sites along c at the same coordinate along a and the z components are alternating, whereas in the latter case the x components are alternating and z components are parallel).

APPENDIX C: MAGNETIC STRUCTURE FACTORS

This section gives the analytic expressions for the magnetic structure factors. Starting from the general expression in (2) we obtain the magnetic structure factors for the F, C, A, and G basis vectors as follows:

$$\mathcal{F}^F(\boldsymbol{Q}) = \begin{cases} 16\boldsymbol{M}_{\pm\boldsymbol{q},1}\cos\frac{\pi l}{6}e^{i\xi_\pm}, & h,k,l \text{ all even and}\\ & h+k+l=4p, \quad p \text{ integer},\\ 16\boldsymbol{M}_{\pm\boldsymbol{q},1}\cos\frac{\pi l}{6}\cos\frac{\pi(h+l-k)}{4}e^{i\chi_\pm}, & \\ & h,k,l \text{ all odd},\\ 0, & \text{otherwise},\end{cases} \tag{C1}$$

$$\mathcal{F}^C(\boldsymbol{Q}) = \begin{cases} 16\boldsymbol{M}_{\pm\boldsymbol{q},1}\cos\frac{\pi l}{6}e^{i\xi_\pm}, & h,k,l \text{ all even and}\\ & h+k+l=4p+2, \quad p \text{ integer},\\ 16\boldsymbol{M}_{\pm\boldsymbol{q},1}\cos\frac{\pi l}{6}\sin\frac{\pi(h+l-k)}{4}e^{i(\chi_\pm+\pi/2)}, & \\ & h,k,l \text{ all odd},\\ 0, & \text{otherwise},\end{cases} \tag{C2}$$

$$\mathcal{F}^A(\boldsymbol{Q}) = \begin{cases} 16\boldsymbol{M}_{\pm\boldsymbol{q},1}\sin\frac{\pi l}{6}e^{i(\xi_\pm-\pi/2)}, & h,k,l \text{ all even and}\\ & h+k+l=4p, \quad p \text{ integer},\\ 16\boldsymbol{M}_{\pm\boldsymbol{q},1}\sin\frac{\pi l}{6}\cos\frac{\pi(h+l-k)}{4}e^{i(\chi_\pm-\pi/2)}, & \\ & h,k,l \text{ all odd},\\ 0, & \text{otherwise},\end{cases} \tag{C3}$$

$$\mathcal{F}^G(\boldsymbol{Q}) = \begin{cases} 16\boldsymbol{M}_{\pm\boldsymbol{q},1}\sin\frac{\pi l}{6}e^{i(\xi_\pm+\pi/2)}, & h,k,l \text{ all even and}\\ & h+k+l=4p+2, \quad p \text{ integer},\\ 16\boldsymbol{M}_{\pm\boldsymbol{q},1}\sin\frac{\pi l}{6}\sin\frac{\pi(h+l-k)}{4}e^{i(\chi_\pm+\pi)}, & \\ & h,k,l \text{ all odd},\\ 0, & \text{otherwise},\end{cases} \tag{C4}$$

where $\xi_\pm = \pi(h+k-3l\pm q)/4$ and $\chi_\pm = \pi(2h-2l\pm q)/4$ and to obtain a closed-form analytic expression we used the "ideal" iridium position $z = 5/8 + 1/12$.

APPENDIX D: AZIMUTH DEPENDENCE OF THE MAGNETIC RESONANT X-RAY DIFFRACTION INTENSITY

Here we obtain the azimuth dependence of the magnetic x-ray diffraction intensity and show how it can be used to determine the relative phase between magnetic basis vectors. As discussed in Sec. III D the magnetic diffraction intensity is proportional to $|\mathcal{F}_\parallel|^2$, where $\mathcal{F}_\parallel = \boldsymbol{\mathcal{F}}\cdot\hat{\boldsymbol{k}}'$ is the projection of the structure factor vector onto the scattered beam direction. To calculate this dot product it is convenient to express both vectors in terms of their components in the laboratory reference frame [25] illustrated in Fig. 9 and defined by the orthonormal set of vectors $\hat{\boldsymbol{U}}_2 = \hat{\boldsymbol{k}}\times\hat{\boldsymbol{k}}'$, $\hat{\boldsymbol{U}}_3 = -\hat{\boldsymbol{Q}}$, and $\hat{\boldsymbol{U}}_1 = \hat{\boldsymbol{U}}_2\times\hat{\boldsymbol{U}}_3$; i.e., $\hat{\boldsymbol{U}}_2$ is normal to the scattering plane and $\hat{\boldsymbol{U}}_1$ is in the scattering plane making an angle θ with both $\boldsymbol{k}$ and $\boldsymbol{k}'$, where 2θ

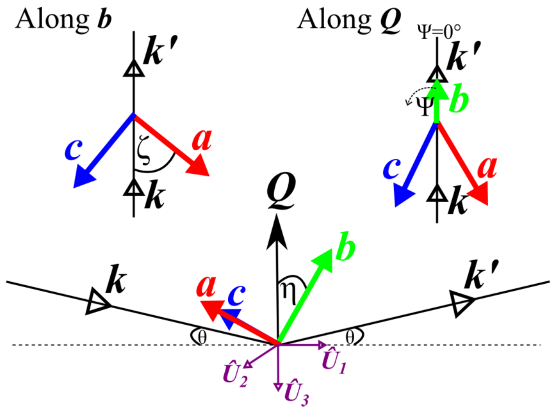

FIG. 9. (Color online) Schematic diagram of the x-ray diffraction experiment at zero azimuth ($\Psi = 0$). $\boldsymbol{k}$ and $\boldsymbol{k}'$ are the incident and scattered x-ray beam wave vectors, and $\boldsymbol{Q} = \boldsymbol{k}' - \boldsymbol{k}$ is the scattering wave vector. The main (bottom) panel shows the orientation of the laboratory frame unit vectors $\hat{\boldsymbol{U}}_{\boldsymbol{1,2,3}}$ and the orthorhombic crystal axes $(\boldsymbol{a},\boldsymbol{b},\boldsymbol{c})$. Top left inset: view along $\boldsymbol{b}$ showing the angle ζ subtended from the scattering plane by the $\boldsymbol{a}$ vector. Right inset: view along $\boldsymbol{Q}$. During an azimuth scan the crystal axes are rotated around $\boldsymbol{Q}$ by an angle Ψ (in the sense shown in the figure); the reference position $\Psi = 0$ is defined as the azimuth angle for which $\boldsymbol{b}$ lies in the scattering plane making the smallest angle with the incident beam direction $\hat{\boldsymbol{k}}$.

is the total scattering angle. The scattered beam direction then can be written as $\hat{\boldsymbol{k}}' = (\cos\theta, 0, -\sin\theta)_L$, where the L subscript indicates that the components are with respect to the laboratory basis of $\hat{\boldsymbol{U}}_{1,2,3}$ vectors, as opposed to the crystal basis, defined by the orthonormal set of vectors $\hat{\boldsymbol{x}}$, $\hat{\boldsymbol{y}}$, $\hat{\boldsymbol{z}}$ (along the orthorhombic axes $\boldsymbol{a}$, $\boldsymbol{b}$, $\boldsymbol{c}$).

The magnetic structure factor vector $\boldsymbol{\mathcal{F}}$ defined in (2) is most naturally expressed in terms of the crystal basis as $(\mathcal{F}_x, \mathcal{F}_y, \mathcal{F}_z)_C$. The components in the laboratory basis $(\mathcal{F}_1, \mathcal{F}_2, \mathcal{F}_3)_L$ are obtained via a linear transformation encoded in a matrix $T(\Psi)$ via

$$\begin{bmatrix}\mathcal{F}_1\\ \mathcal{F}_2\\ \mathcal{F}_3\end{bmatrix} = T(\Psi)\begin{bmatrix}\mathcal{F}_x\\ \mathcal{F}_y\\ \mathcal{F}_z\end{bmatrix}, \tag{D1}$$

where we have explicitly introduced the dependence of the transformation matrix on the azimuth angle Ψ, which defines the rotation angle of the crystal axes around the scattering wave vector $\boldsymbol{Q}$. To find the transformation matrix we first consider the reference position of zero azimuth, $\Psi = 0$, depicted in Fig. 9. In this case the orientation of the crystal axes with respect to the laboratory axes is specified by two angles η and ζ. η is the angle between the $\boldsymbol{b}$ axis and the scattering wave vector $\boldsymbol{Q}$, given by

$$\eta = \cos^{-1} \hat{\boldsymbol{Q}} \cdot \hat{\boldsymbol{b}}$$

and ζ is the angle between the $\boldsymbol{a}$-axis and the scattering plane, given by

$$\zeta = \tan^{-1} \frac{\boldsymbol{Q} \cdot \hat{\boldsymbol{c}}}{\boldsymbol{Q} \cdot \hat{\boldsymbol{a}}}.$$

Using the diagram in Fig. 9 the transformation matrix is obtained as

$$T(0) = \begin{bmatrix} -\cos\zeta\cos\eta & \sin\eta & -\sin\zeta\cos\eta \\ \sin\zeta & 0 & -\cos\zeta \\ -\cos\zeta\sin\eta & -\cos\eta & -\sin\zeta\sin\eta \end{bmatrix}. \tag{D2}$$

When moving away from the reference position to a finite azimuth angle Ψ the coordinates in the laboratory frame need to be multiplied by the rotation matrix

$$R(\Psi) = \begin{bmatrix} \cos\Psi & \sin\Psi & 0 \\ -\sin\Psi & \cos\Psi & 0 \\ 0 & 0 & 1 \end{bmatrix}, \tag{D3}$$

such that the resulting transformation matrix from the crystal to the laboratory bases in (D1) becomes

$$T(\Psi) = R(\Psi)T(0). \tag{D4}$$

Explicitly, substituting (D2) and (D3) into (D4) yields

$$T(\Psi) = \begin{bmatrix} \sin\Psi\sin\zeta - \cos\Psi\cos\zeta\cos\eta & \cos\Psi\sin\eta & -\cos\Psi\sin\zeta\cos\eta - \sin\Psi\cos\zeta \\ \sin\Psi\cos\zeta\cos\eta + \cos\Psi\sin\zeta & -\sin\Psi\sin\eta & \sin\Psi\sin\zeta\cos\eta - \cos\Psi\cos\zeta \\ -\cos\zeta\sin\eta & -\cos\eta & -\sin\zeta\sin\eta \end{bmatrix}. \tag{D5}$$

Once the structure factor components are obtained in the laboratory basis, then the projection of the structure factor vector along the scattered beam direction is readily obtained as

$$\mathcal{F}_\parallel = \cos\theta\,\mathcal{F}_1 - \sin\theta\,\mathcal{F}_3. \tag{D6}$$

To illustrate the azimuth dependence of the magnetic x-ray diffraction intensity we consider the magnetic peak at $(-6,6,8)+\boldsymbol{q}$ in Fig. 5(a). Here only the A_x and F_z basis vectors contribute, therefore $\boldsymbol{\mathcal{F}} = (\mathcal{F}_x, 0, \mathcal{F}_z)_C$ where the structure factor components $\mathcal{F}_x$ and $\mathcal{F}_z$ are of the types $\mathcal{F}^A$ and $\mathcal{F}^F$ in (C3) and (C1), respectively. Using (D6) combined with (D1) and (D5) we obtain

$$\mathcal{F}_\parallel(\Psi) = g_x(\Psi)\mathcal{F}_x + g_z(\Psi)\mathcal{F}_z,$$

where the geometric factors are

$$\begin{aligned} g_x(\Psi) &= (\sin\Psi\sin\zeta - \cos\Psi\cos\zeta\cos\eta)\cos\theta \\ &\quad + \cos\zeta\sin\eta\sin\theta, \\ g_z(\Psi) &= \sin\zeta\sin\eta\sin\theta \\ &\quad - (\cos\Psi\sin\zeta\cos\eta + \sin\Psi\cos\zeta)\cos\theta. \end{aligned}$$

The magnetic scattering intensity is then proportional to

$$\begin{aligned} |\mathcal{F}_\parallel(\Psi)|^2 &= |g_x(\Psi)\mathcal{F}_x|^2 + |g_z(\Psi)\mathcal{F}_z|^2 \\ &\quad + 2\,\mathrm{Re}(\mathcal{F}_z\mathcal{F}_x^*)g_x(\Psi)g_z(\Psi), \end{aligned}$$

where Re() means the real part. The first two terms give the sum of the separate contributions from the two basis vectors, whereas the last (cross-term) is sensitive to the relative phases between the two basis vectors. Using Eqs. (C1) and (C3), the cross-term is proportional to

$$\mathcal{F}_z\mathcal{F}_x^* \propto \begin{cases} \mp i \sin\frac{\pi l}{6}\cos\frac{\pi l}{6}, & F_z \pm A_x, \\ \pm \sin\frac{\pi l}{6}\cos\frac{\pi l}{6}, & F_z \pm iA_x. \end{cases}$$

The cross-term is therefore directly sensitive to the phase difference between the two contributing basis vectors. If F_z and A_x are in phase or π out of phase (denoted as $F_z \pm A_x$) the product $\mathcal{F}_z\mathcal{F}_x^*$ is purely imaginary, so the cross-term cancels and the intensity is given by the sum of the contributions from the two basis vectors taken separately. This is clearly inconsistent with the data [purple curve in Fig. 5(a)]. A phase difference of $\pm\pi/2$ between the two basis vectors (denoted as $F_z \pm iA_x$) gives a finite cross-term, which changes sign between those two cases, and the data in Fig. 5(a) identifies the basis vector combination as $F_z + iA_x$ (red solid line).

APPENDIX E: MAPPING OF MAGNETIC BASIS VECTORS BETWEEN β- AND γ-Li_2IrO_3

In this section we describe a formal mapping of the magnetic basis vectors between the notation used for the β (space group $Fddd$) and γ (space group $Cccm$) polytypes of Li_2IrO_3. The iridium lattice arrangement in both crystal

TABLE VI. Equivalence between the iridium sites in γ-Li_2IrO_3 ($Cccm$ space group) with those in β-Li_2IrO_3 ($Fddd$ space group) (when both are projected onto the ac plane). Last column shows additional translations to be applied to primitive lattice sites in the $Fddd$ structure (column 2) in addition to a common translation by $(-1/8,0,1/8)$ to get the positions in the $Cccm$ structure (column 1). For each structure the "ideal" iridium positions have been used.

Site $Cccm$	Site $Fddd$	Translation
1	4	$-(0,0,1)$
2	3	$(0,0,0)$
3	3	$(0,1/2,1/2)$
4	4	$-(0,1/2,1/2)$
$1'$	2	$(1/2,1/2,0)$
$2'$	1	$(1/2,0,-1/2)$
$3'$	1	$(1/2,1/2,0)$
$4'$	2	$(1/2,1,1/2)$

TABLE VII. Mapping of magnetic basis vectors between the $Fddd$ and $Cccm$ notations.

Basis vector $Fddd$ (4-site, [1-4])	Basis vector $Cccm$ (8-site, [1-4, $1'$-$4'$])
$A\ [+--+]$	$(A,-A)\ [+--+,-++-]$
$C\ [++--]$	$(-F,F)\ [----,++++]$
$F\ [++++]$	$(F,F)\ [++++,++++]$
$G\ [+-+-]$	$(-A,-A)[-++-,-++-]$

structures is made up of zigzag chains vertically linked along the c axis, with the only difference being that in the β polytype successive chains along c alternate in orientation between the $\boldsymbol{a} \pm \boldsymbol{b}$ directions, whereas in the γ polytype a pair of successive chains are parallel and this direction then alternates for the next pair of parallel chains and so on, between the $\boldsymbol{a} \pm \boldsymbol{b}$ directions. When both structures are viewed in projection onto the ac plane [as shown in Fig. 6(a) and Fig. 4 of Ref. [20]] the two iridium lattice arrangements then look identical. This suggests that a formal mapping can be constructed between the notations used to describe the sites of the primitive cells of the two materials, and also between the magnetic basis vectors, such that one can then describe a magnetic structure equivalently in the notation of one or the other space group (of course the magnetic structures would only be "equivalent" up to the projection of the sites onto the b axis). Table VI lists the equivalence between the sites in the primitive cell of the two structures (up to the y coordinate of sites), where for the γ polytype we follow the notation in Ref. [20] (two iridium sublattices with sites 1-4 and $1'$-$4'$). Using this site equivalence one can construct a mapping of the magnetic basis vectors as listed in Table VII. The magnetic structure described by the basis vector combination (iA_x, iC_y, F_z) in the $Fddd$ setting then corresponds, in the notation of the $Cccm$ setting, to $i(A,-A)_x, i(-1)^m(F,-F)_y,(F,F)_z$ with $m = 1$.

[1] For a review see W. Witczak-Krempa, G. Chen, Y. B. Kim, and L. Balents, Annu. Rev. Condens. Matter Phys. **5**, 57 (2014).

[2] B. J. Kim, H. Ohsumi, T. Komesu, S. Sakai, T. Morita, H. Takagi, and T. Arima, Science **323**, 1329 (2009).

[3] G. Jackeli and G. Khaliullin, Phys. Rev. Lett. **102**, 017205 (2009).

[4] J. Chaloupka, G. Jackeli, and G. Khaliullin, Phys. Rev. Lett. **105**, 027204 (2010).

[5] A. Kitaev, Ann. Phys. (NY) **321**, 2 (2006).

[6] J. Knolle, D. L. Kovrizhin, J. T. Chalker, and R. Moessner, Phys. Rev. Lett. **112**, 207203 (2014).

[7] Y. Singh and P. Gegenwart, Phys. Rev. B **82**, 064412 (2010).

[8] X. Liu, T. Berlijn, W.-G. Yin, W. Ku, A. M. Tsvelik, Y.-J. Kim, H. Gretarsson, Y. Singh, P. Gegenwart, and J. P. Hill, Phys. Rev. B **83**, 220403(R) (2011).

[9] S. K. Choi, R. Coldea, A. N. Kolmogorov, T. Lancaster, I. I. Mazin, S. J. Blundell, P. G. Radaelli, Yogesh Singh, P. Gegenwart, K. R. Choi, S.-W. Cheong, P. J. Baker, C. Stock, and J. Taylor, Phys. Rev. Lett. **108**, 127204 (2012).

[10] F. Ye, S. Chi, H. Cao, B. C. Chakoumakos, J. A. Fernandez-Baca, R. Custelcean, T. F. Qi, O. B. Korneta, and G. Cao, Phys. Rev. B **85**, 180403(R) (2012).

[11] H. Gretarsson, J. P. Clancy, Y. Singh, P. Gegenwart, J. P. Hill, J. Kim, M. H. Upton, A. H. Said, D. Casa, T. Gog, and Y.-J. Kim, Phys. Rev. B **87**, 220407(R) (2013).

[12] M. J. O'Malley, H. Verweij, and P. M. Woodward, J. Solid State Chem. **181**, 1803 (2008).

[13] Y. Singh, S. Manni, J. Reuther, T. Berlijn, R. Thomale, W. Ku, S. Trebst, and P. Gegenwart, Phys. Rev. Lett. **108**, 127203 (2012).

[14] S. Mandal and N. Surendran, Phys. Rev. B **79**, 024426 (2009).

[15] Eric Kin-Ho Lee, R. Schaffer, S. Bhattacharjee, and Y. B. Kim, Phys. Rev. B **89**, 045117 (2014).

[16] I. Kimchi, J. G. Analytis, and A. Vishwanath, arXiv:1309.1171.

[17] E. K.-H. Lee and Y. B. Kim, arXiv:1407.4125.

[18] T. Takayama, A. Kato, R. Dinnebier, J. Nuss, and H. Takagi, arXiv:1403.3296.

[19] K. A. Modic, T. E. Smidt, I. Kimchi, N. P. Breznay, A. Biffin, S. Choi, R. D. Johnson, R. Coldea, P. Watkins-Curry, G. T. McCandless, J. Y. Chan, F. Gandara, Z. Islam, A. Vishwanath, A. Shekhter, R. D. McDonald, and J. G. Analytis, Nat. Commun. **5**, 4203 (2014).

[20] A. Biffin, R. D. Johnson, I. Kimchi, R. Morris, A. Bombardi, J. G. Analytis, A. Vishwanath, and R. Coldea, Phys. Rev. Lett. **113**, 197201 (2014).

[21] S. Boseggia, R. Springell, H. C. Walker, H. M. Rønnow, Ch. Rüegg, H. Okabe, M. Isobe, R. S. Perry, S. P. Collins, and D. F. McMorrow, Phys. Rev. Lett. **110**, 117207 (2013).

[22] J. Rodriguez-Carvajal, Physica B **192**, 55 (1993).

[23] S. C. Miller and W. F. Love, *Tables of Irreducible Representations of Space Groups and Co-Representations of Magnetic Space Groups* (Pruett, Boulder, 1967).

[24] M. Blume and D. Gibbs, Phys. Rev. B **37**, 1779 (1988).

[25] J. P. Hill and D. F. McMorrow, Acta Crystallogr. A **52**, 236 (1996).

[26] C. Detlefs, M. Sanchez del Rio, and C. Mazzoli, Eur. Phys. J. Spectrosc. Top. **208**, 359 (2012).

[27] http://forge.ill.eu/svn/magnetix.

[28] S. Choi, R. Coldea *et al.* (unpublished).

[29] ISOTROPY software suite, http://iso.byu.edu.